ELSEVIER

A COMPLEMENTAL ANALYSIS OF WAVE IRREGULARITY EFFECT ON THE HYDRODYNAMIC RESPONSES OF OFFSHORE WIND TURBINES WITH THE SEMI-SUBMERSIBLE PLATFORM

Y.R. Alkarem, B.O. Ozbahceci[*]

İzmir Institute of Technology, Faculty of Engineering, Department of Civil Engineering, 35430, Urla, Izmir, Turkey

ARTICLE INFO

ABSTRACT

Changes in the spectral shape and the directional spreading are typical properties of irregular waves in nature. The effect of wave irregularity on the hydrodynamic responses of floating offshore wind turbines (FOWT) has been investigated in several studies. However, a complemental analysis of the effects of frequency spectrum shape and wave multi-directionality on the low-frequency (LF) and the wave-frequency (WF) responses due to the second order and the first order hydrodynamic loads, respectively and cable tensions of FOWT under a complete range of mean wave directions is missing. In this study, two hydrodynamic models are developed firstly using different calibration methods based on the free decay tests and wave loading tests. They are compared with the experimental data for validation. No wind loads were considered in this analysis. The validation results show that the model calibrated using wave loading has better agreement with the experimental data, especially in the LF region, and therefore used for further analysis. Then the hydrodynamic responses are investigated under irregular waves with different spectral shapes. As the spectral shape becomes narrower with pronounced wave grouping and the larger waves in the time series, the responses and tensions increase in the WF region. Furthermore, the narrower the spectrum, the more snap loads in the mooring cables occur. Hydrodynamic responses are also compared under a uni-directional and multi-directional wave excitation from all angles of attack in terms of LF and WF amplitudes. The condition that the responses under multi-directional waves are higher than the ones under uni-directional waves has appeared in multiple cases, especially in the WF region, although it does not lead to excessive responses like the uni-directional wave. Therefore, it is concluded that the wave irregularity in terms of the spectral shape and the directional spreading should be considered during the design stage for better comprehension of the actual motion of floating wind turbines.

1. Introduction

The offshore wind industry is foreseen to be highly potent to decarbonize the energy industry. A wind farm situated offshore encounters 90% greater wind on average than an onshore wind farm (Archer & Jacobson, 2005). Walsh (2019) shows that offshore wind farms move gradually from the coastline in Europe since the beginning of the 21st century and their average water depth increases to 60 meters. As water depth increases, the shift of wind turbine foundations from being fixed to floating is gradually gaining pace in the wind industry. Therefore, the demand to capture the accurate responses of the floating offshore wind turbines (FOWT) is high.

Computer-aided Engineering tools are widely used to develop

numerical models to estimate linear and non-linear responses of FOWT systems such as the aero-hydro-servo-elastic FAST code (Jonkman & Buhl, 2005). Some scholars have devised simplified aero-hydro dynamic models to produce fast results at the expense of accuracy (Karimirad & Moan, 2012; Kim et al., 2015), while others use CFD-based models to improve accuracy at the expense of the computational cost (Benitz et al., 2015; Tran & Kim, 2018). If this to be avoided, hydrodynamic effects can be investigated by applying potential-flow or Morison's equation-based approaches. The former neglects viscous-induced excitation/damping, while the latter is inapplicable for large diffracting structures. These limitations must be considered to capture the accurate response of the structure. A good approach is to use both models simultaneously to avoid excessive computational time. A recent study by
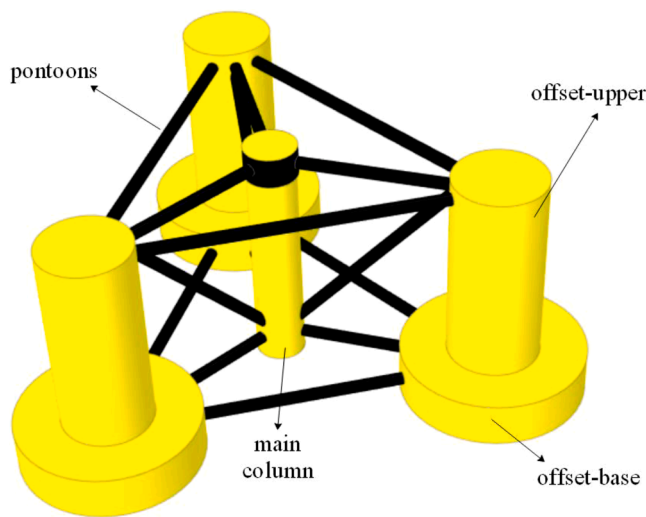
Fig. 1. Semi-submersible floating platform geometry

Table 1
Gross System properties

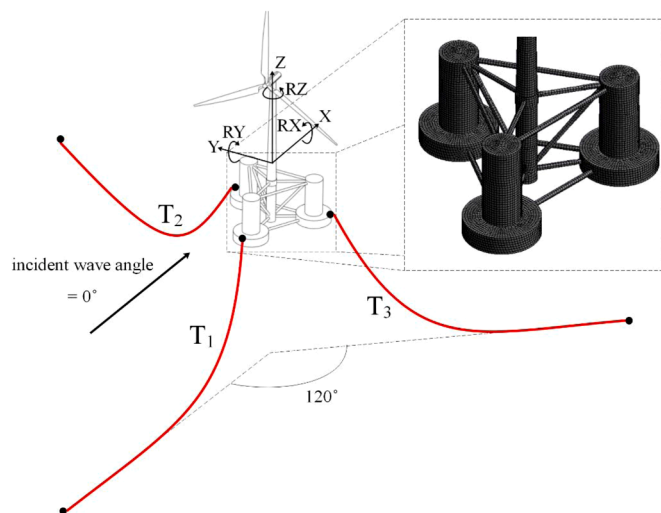| Property	Value
Mass	$1.4079 \times 10^7 \mathrm{kg}$
Draft	20 m
Air gap	10 m
Volumetric Displacement	13,988 m³
Center of mass below sea water level	14.4 m
Roll inertia about the system's center of mass	$1.099 \times 10^{10} \mathrm{kg \cdot m^2}$
Pitch inertia about the system's center of mass	$1.099 \times 10^{10} \mathrm{kg \cdot m^2}$
Yaw inertia about the system's center of mass	$1.908 \times 10^{10} \mathrm{kg \cdot m^2}$

Fig. 2. The geometry of the moored semi-submersible FOWT system together with the meshed platform

Liu et al. (2020) is an example of utilizing this approach for the experimental and numerical investigation of a semi-submersible aquaculture facility. Tensions in the mooring can be modeled using either quasi-static or dynamic modeling. However, while the quasi-static model contributes to accurate static tension values, it results in under-predicting the tensions in the cables under dynamic motion. In fact, the dynamic model is more appropriate to capture the dynamic

behavior of the cables (Masciola et al., 2013). Nevertheless, even if a dynamic model is employed, cables are driven by the motion of fairleads, which, in turn, is driven by wind and wave-induced excitations. Therefore, erroneous prediction of structural response subsequently influences the tension values (Hall & Goupee, 2015), but the influence of tension dynamics on the floating wind turbine's global performance outside snap load events is insignificant (Masciola et al., 2013).

In most of the numerical and experimental studies on FOWT, as explained above, regular waves or uni-directional irregular waves with a constant spectrum shape have been used. However, various observations show that the frequency spectrum shape is not constant. Change in the frequency spectrum may pronounce the wave grouping and extreme waves in a time series[nullU]. Therefore, change in the spectrum shape might influence slowly-varying responses at the low-frequency (LF) and the responses at the wave-frequency (WF) region of FOWT. However, this has only been narrowly investigated in the literature. Saulnier et al. (2011) have underlined the essential role of wave grouping and the standard wave parameters (wave height and period) on the behavior of the wave energy converters and, consequently, on the power production estimation. Barrera et al. (2019) have studied the significance of wave parameters over the mooring dynamics in severe sea states and have demonstrated that maximum tensions are not dependent on maximum wave heights but instead on the sequence of waves. Li and Zhang (2020) investigated the fatigue damage on spar type floating wind turbine based on sensitivity analysis of elementary wind- and wave-related parameters.

The spreading of the energy into a broader range of directions is another form of wave irregularity, unlike the commonplace application of uni-directional waves. Kvittem and Moan (2015) studied fatigue forces on a semi-submersible platform under misaligned wind and wave excitations and concluded that the assumption of uni-directionality is conservative, but the tremendous fatigue damage is a function of the wave direction. Zhang and Ishihara (2016) concluded that when numerically testing the spreading effect on the Fukushima MIRAI 2MW FWT prototype, multi-directional waves decrease the motion in surge, heave, and pitch. On the other hand, Waals (2009) derived a 4-dimensional quadratic transfer function (QTF) related to the wave of different frequencies and directions for calculating a soft-moored ship's LF motions. He found that wave directionality may significantly impact the vessel motion, especially in shallow water and that conventional simulations are not conservative, particularly of motions not excited by uni-directional loading. The same conclusion was reached by Duarte et al. (2014) after they used an equal-energy discretization method in synthesizing multi-directional wave time series and tested the effect of multi-directional waves on a semi-submersible platform and detected a significant increase in sway and roll motion. It should be noted here that the wave incidence's alignment with the surge axis of the FOWT has been considered in these studies. Abou-Rayan et al. (2016) investigated the dynamic behavior of TLP's supporting 5-MW wind turbines under irregular wave conditions with various wave angles, but the waves were uni-directional.

The literature study summarized above shows a complemental analysis of the triggering and weakening effects of frequency spectrum shape and wave multi-directionality on LF, WF responses, and cable tensions of FOWT under various mean wave directions is missing. This paper proposes a numerical model that captures non-linear effects and addresses wave irregularity influences after calibrating and validating the hydrodynamic and mooring dynamics of the FOWT (aerodynamics are not included) for better comprehension of the motion of floating wind turbines under a wide range of irregular wave loading. The platform under study is the DeepCwind semi-submersible studied in phase II of the Offshore Code Comparison Continued, with Correlation (OC5) Project(Robertson et al., 2017).

The remaining of the paper is constructed as follows; Section 2 describes the numerical model setup. Two calibration schemes and their validation against the physical model measurements are given in Section

Table 2
Chain and catenary line properties

Property	Symbol	Value
Pretension	T_0	1,124 kN
unstarched length	L_c	833.60 m
Young's modulus of Elasticity	E	$5.44 \times 10^4 \text{kN/m}^2$
axial stiffness	EA	$7.6432 \times 10^5 \text{ kN/m}^2$
mass per unit length	m	116.6 kg/m
steel density	ρ_s	8,298 kg/m³
nominal diameter	d_c	0.079 m
equivalent diameter	D_c	0.1337 m
nominal normal drag coefficient	C_{dn_0}	2.4
nominal tangential drag coefficient	C_{dt_0}	1.15
nominal normal added mass coefficient	C_{a0}	1.0
scaled normal drag coefficient	C_{dn}	1.30
scaled tangential drag coefficient	C_{dt}	0.21
scaled normal added mass coefficient	C_a	0.58

3. Section 4 illustrates the influence of frequency spectrum shape on the system response and the correlation between LF and WF motions. Furthermore, Section 5 highlights the relative significance of excitation under uni-directional and multi-directional wave loading assumptions. Conclusions of the results and possible future work are discussed in Section 6.

2. Numerical Model Set-up

The 5-MW rated baseline wind turbine designed by NREL is used in the model. Its gross properties are described by Jonkman et al. (2009). The floating platform under study is the DeepCwind semi-submersible shown in Fig. 1, studied in phase II of the OC5 Project (Robertson et al., 2017). The platform is a hybrid design that adapts buoyancy as the primary stability method but uses ballast to lower the center of gravity for better restoring moments. Three catenary mooring lines are attached to the base columns for station-keeping purposes. The platform properties are slightly different from DeepCwind semi-submersible and are given in Table 1. The geometry of the moored system together with the meshed platform is presented in Fig. 2, and the mooring properties are provided in Table 2. The reader is referred to (Robertson et al., 2014, 2016) for a complete description of the system.

ANSYS™ AQWA® package is used as the central element of the numerical simulation. The software can model the coupled motions of all six degrees of freedom (DOF) of floating structures under the influence of gravitational, hydrostatic, hydrodynamic, wind, mooring, and current loads either in the frequency-domain (FD) for rapid evaluation (valid for the initial stages of a new design) or in the more rigorous time-domain (TD) analysis (ANSYS Inc., 2013). The global equation of motions for one structure in FD and TD, respectively, are written as:

$$\left[-\omega^2 \mathbf{M} - i\omega \mathbf{C} + \mathbf{K} \right] \mathbf{X}(\omega) = \mathbf{F}(\omega) \tag{1}$$

$$\mathbf{M}\ddot{\mathbf{X}}(t) + \mathbf{C}\dot{\mathbf{X}}(t) + \mathbf{K}\mathbf{X}(t) = \mathbf{F}(t) \tag{2}$$

where; $\mathbf{M}$ is the assembled structural mass and added mass matrix, $\mathbf{C}$ is the damping matrix and $\mathbf{K}$ is the total stiffness of the system including the linear hydrostatic stiffness coupled with the additional stiffness from the mooring lines, and $\mathbf{F}$ is the 6×1 matrix containing the combination of all external forces as a function of frequency ω or time t. In TD, AQWA uses a semi-implicit two-stage predictor-corrector scheme by integrating in time displacement $\mathbf{X}$ and velocity $\dot{\mathbf{X}}$ matrices to solve for the acceleration $\ddot{\mathbf{X}}$ matrix.

The hydrodynamic model employs a three-dimensional radiation/diffraction panel theory and Morison's equation. The second order wave forces are solved by considering pairs of sinusoidal waves of frequencies (ω_i;ω_j), wave amplitude of (a_i;a_j), and phase shifts of (ε_i;ε_j):

$$F_{i,j}^{(2)}(t) = \text{Re}\left\{ \sum_i \sum_j a_i a_j T_\alpha(\omega_i; \omega_j) e^{-i[\omega_i - \omega_j]t + \varepsilon_i - \varepsilon_j} \right\} \tag{3}$$

where $T_\alpha(\omega_i;\omega_j)$ is the amplitude of second order force per unitary pair of wave amplitudes and is known as the quadratic transfer function (QTF). When $\omega_i = \omega_j$, the corresponding wave force is constant mean drift force, and the difference frequency $\omega_i - \omega_j$ brings forth the slowly varying motions. These two types of forces constitute the LF component of the response.

The mooring system can be modeled using a quasi-static model or a dynamic model. A quasi-static solution ignores the dynamic drag and inertia wave forces acting on the cable. Hence, the mooring-induced force on the platform in the jth platform DOF is written as:

$$F_j^{lines} = F_j^{lines,0} - k_{jj_m} X_j \tag{4}$$

where; $F_j^{lines,0}$ is the net force at the platform's undisplaced position, k_{jj_m} is the jth stiffness contributed by the mooring connections, and X_j is j^{th} platform DOF. Jonkman (2007) formulated an elastic catenary cable's analytical solution suspended in the fluid between the anchor and the fairlead. When a portion of the cable lies on the seabed, and if the cable's physical characteristics are given, then the two unknowns – the horizontal and vertical tension at the fairlead (T_H; T_V) can be solved for through these equations (origin here is at the anchor position):
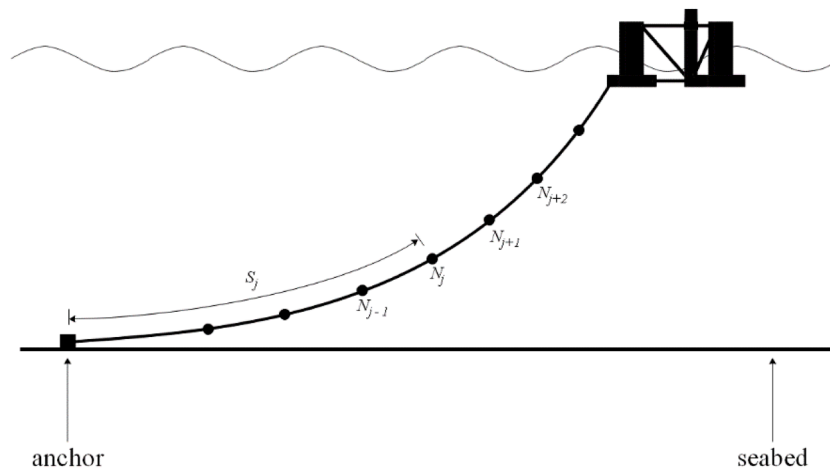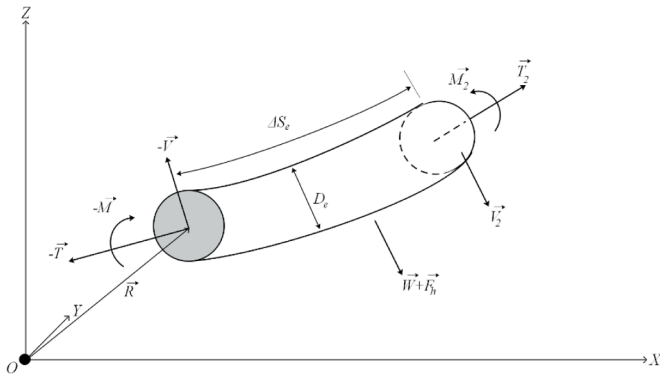

Fig. 3. Cable discretization
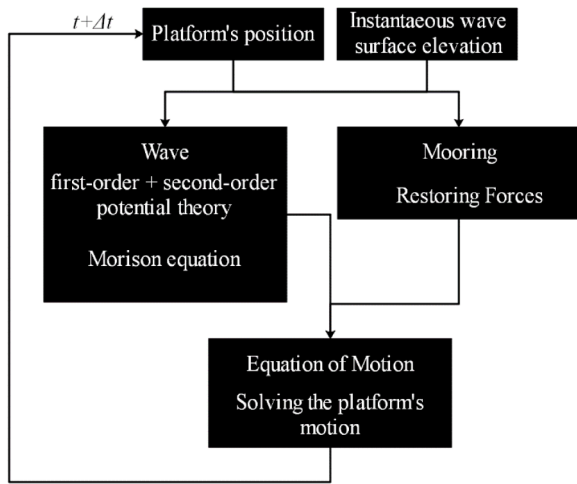
Fig. 4. Single Morison element (ANSYS Inc., 2013)

Fig. 5. flow chart of the coupling methodology

Table 3
Load cases

Load Case	Description	Usage	Conditions	Duration [s]
LC 1	free decay tests	Calibration	$X_0^* = 6.30$ m	1000
			$Y_0 = 6.30$ m	1000
			$Z_0 = 2.13$ m	300
			$RX_0 = 4.00$ deg	300
			$RY_0 = 4.00$ deg	300
			$RZ_0 = 11.20$ deg	900
LC 2	moderate regular wave	Calibration	$H = 7.37$ m, $T = 12.07$ s	1,000
LC 3	moderate irregular wave	Calibration	JONSWAP spectrum $H_s = 7.10$ m, $T_p = 12.10$ s, $\gamma = 2.2$	11,534
LC 4	extreme regular wave	Validation	$H = 9.41$ m, $T = 14.30$ s	1,000
LC 5	extreme irregular wave	Validation	JONSWAP spectrum $H_s = 10.50$ m, $T_p = 14.30$ s, $\gamma = 3.0$	11,774
LC 6	white noise	Validation	$H_s = 10.50$ m, $T_{range} = 6 - 26$ s	10,774

*The subscript ($_0$) denotes initial transient in the given degree of freedom.

$$x_f(T_H, T_V) = L_c - \frac{T_V}{\omega} + \frac{T_H}{\omega}\sinh^{-1}\frac{T_V}{T_H} + \frac{T_H L_c}{EA} \tag{5}$$

$$z_f(T_H, T_V) = \frac{T_H}{\omega}\left[\sqrt{1 + \left(\frac{T_V}{T_H}\right)^2} - 1\right] + \frac{1}{2EA}\left(\frac{T_V^2}{\omega}\right) \tag{6}$$

The first two terms of Eq. (5) form the laid length $L_B = L_c - T_V/\omega$, where; L_c is the cable's length. x_f and z_f are the horizontal and vertical coordinates of the fairlead position, EA is the axial stiffness of the mooring cable, and ω is its weight per unit length.

When the cable dynamics are solved, the mooring cable is discretized, as seen in Fig. 3, and the effects of the cable mass, drag forces, inline elastic tension, and bending moment are considered. Each portion is dealt with as a Morison element over which hydrodynamic wave forces are projected. A single element is shown in Fig. 4. Neglecting bending stiffness, the equation of motion of an element i is given by:

$$\frac{\partial \overrightarrow{T}}{\partial s_e} + \frac{\partial \overrightarrow{V}}{\partial s_e} + \overrightarrow{\omega} + \overrightarrow{F_h} = m\frac{\partial^2 \overrightarrow{R}}{\partial t^2} \tag{7}$$

where; $\overrightarrow{V}$ and $\overrightarrow{R}$ are the shear force vector and position vector at the initial node of the element, respectively. $\Delta s_e = \overrightarrow{R}_{j+1} - \overrightarrow{R}_j$ is the length of the Morison element, m is the structural mass per unit length, and $\overrightarrow{F_h}$ is the combination of the hydrodynamic forces. Tension vector $\overrightarrow{T}$ is a function of the axial stiffness of the cable:

$$T = EA\varepsilon \tag{8}$$

where; ε is the axial strain.

When applying the appropriate boundary conditions, the cable's dynamic response is solved numerically using the Lump-Mass model. As for the hydrodynamic forces, the wave kinematic component on the mooring dynamics is not included. The time-dependent hydrodynamic forces consist of the buoyant force F_B, drag force F_d, and inertial forces:

$$F_h = F_B + F_d - m_a\left[\overrightarrow{a}_j, \overrightarrow{a}_{j+1}\right]^T \tag{9}$$

where; m_a is the elementary added mass, and $\overrightarrow{a}_j$ is the acceleration at the jth node.

Forces on each element of the discretized cable are quantified and integrated in time. The mooring solution is fully coupled with the floater analysis. The cable tensions and the platform motions are regarded as mutually interactive, where cables affect platform motion and vice versa. The flow chart in Fig. 5 describes the coupling technique.

3. Calibration and Validation Procedure

After setting up the FOWT model, two hydrodynamic models are developed and they are calibrated with different methods. Then, they are tested and compared with the experimental data for validation. OC5 experimental data of a 1/50th-scale tested at the Maritime Research Institute Netherlands offshore wave basin are used in the validation study. Table 3 presents all the load cases used for calibration and validation purposes in this study.

3.1. Description of Hydrodynamic Models

The two hydrodynamic models have some mutual settings. They both utilize the full solution of the quadratic transfer function (QTF) to estimate the potential second order excitations according to the approach described by Pinkster (1980).

The mooring settings in both models are identical as well. Some properties are adjusted according to the data given in Hall and Goupee (2015). However, unlike in the reference, all catenary lines have equal
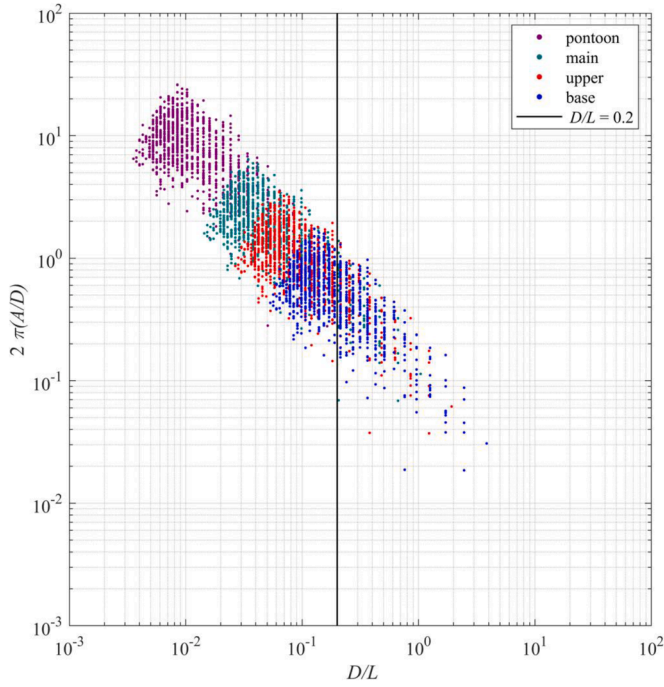
Fig. 6. Classification of wave forces on the platform column

properties to preserve the system's static equilibrium. Table 2 provides the mooring line sectional properties calculated according to DNV GL (2015) and Ulverston et al. (2010). The normal drag coefficient, C_{dn_0} is scaled as in Hall & Goupee (2015) to account for 1) the volume-equivalent diameter, D_c to the nominal diameter, d ratio and 2) the frontal area ratio between the typical chain, $A_{L,typical}$ and the one used in the test, $A_{L,tested}$ as given below:

$$C_{dn} = C_{dn_0} \frac{A_{L,tested}}{A_{L,typical}} \frac{D_c}{d_c} \tag{10}$$

Diffraction effects are important when the ratio of the effective diameter, D of the columns to the wavelength, L is above 0.2. Furthermore, as Keulegan-Carpenter number, $KC = 2\pi(A/D)$ increases, flow separation occurs, leading to viscous drag forces (Robertson et al. 2014). As it is shown in Fig. 1, the floating platform is composed of various parts like the pontoon rings, main column, upper and base

columns with different D values. In order to check whether diffraction forces or viscous forces are effective on the platform parts, D/L ratio is plotted against the Keulegan-Carpenter number together with a limiting D/L ratio of 0.2 for the irregular moderate wave case (LC 3), as shown in Fig. 6. This analysis reveals that small parts of the platform, such as the pontoon rings and the main column, must be modeled as Morison elements. As for the upper and base columns, they overlap both regions. Therefore, the two models diverge in their calculation of the hydrodynamic forces acting on the large structures. They also differ in the calibration method used in each model. Description of the models are given below:

- Mod.1:

Large columns i.e. the upper and base columns of the floating platform are modeled as diffracting elements in the first model, Mod1. The structural damping is calibrated through free Decay Tests (FDT) by providing linear and quadratic damping matrices for all 6 DOF, which is a well-known practice in the literature (for example, Gueydon et al. 2014; A. Robertson et al. 2014; Yang et al. 2021). The diagonal linear and quadratic damping forces are proportional to the velocity and the velocity square, respectively;

$$F_{linear\,ii} = -C_{p_{ii}}\dot{X}_i \tag{11}$$

$$F_{quadratic\,ii} = -C_{q_{ii}}\dot{X}_i \left| \dot{X}_i \right|, \quad i = 1, 2, \ldots 6 \tag{12}$$

Table 4

Diagonal linear (C_p) and quadratic damping (C_q) coefficients used in mod.1

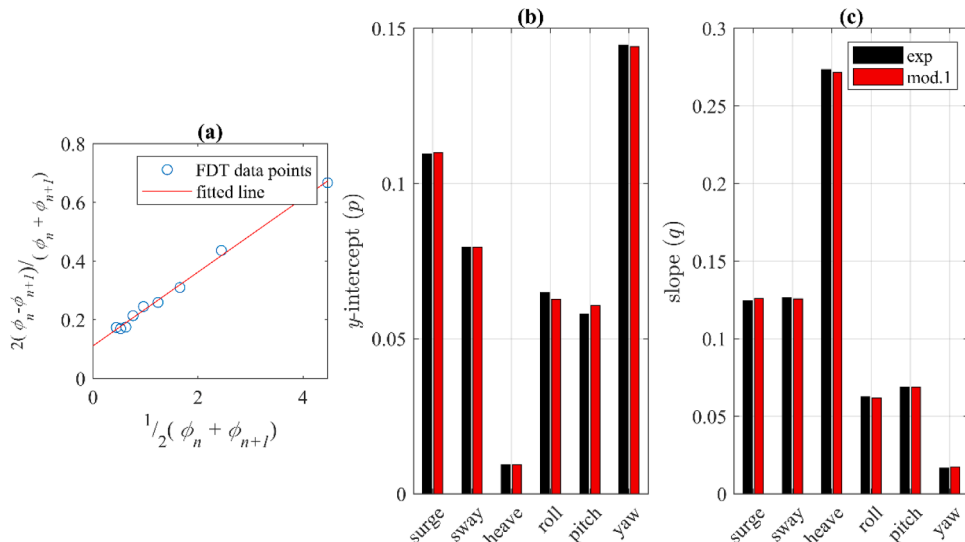| DOF	Linear C_p	Unit	quadratic C_q	unit
surge	3.2×10^4	N/(m/s)	6.6×10^5	N/(m/s)^2
sway	1.8×10^4		7.0×10^5	
heave	0		1.4×10^6	
roll	1.7×10^6	N·m/(deg/s)	2.2×10^6	N·m/(deg/s)^2
pitch	1.4×10^6		3.7×10^6	
yaw	1.2×10^6		1.7×10^6	

Fig. 7. Linear and quadratic damping analysis

Table 5
Coefficient selection for the two calibration schemes

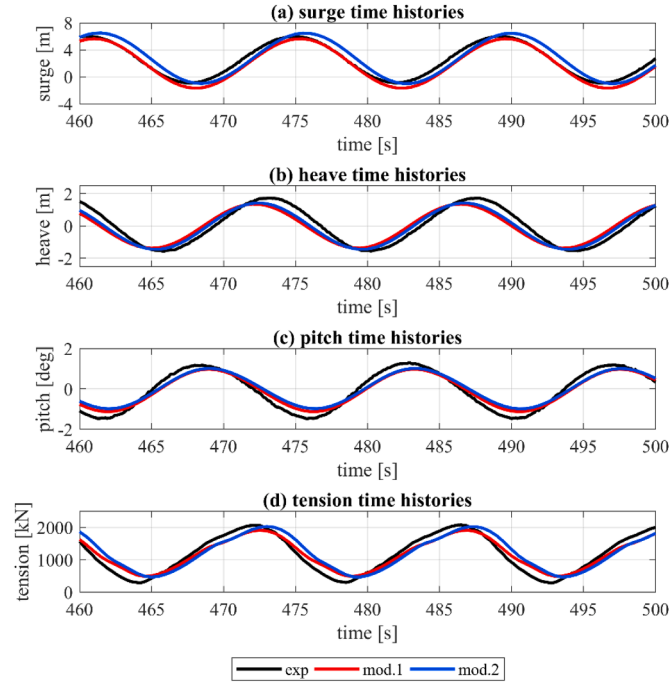| Coefficient	mod.1	mod.2
$C_{d,wk}$	1.00	1.00
μ_c	1.26	0.25
$C_{d,\nu}$	0.00	0.84
$C_{d,z}$	0.00	4.80

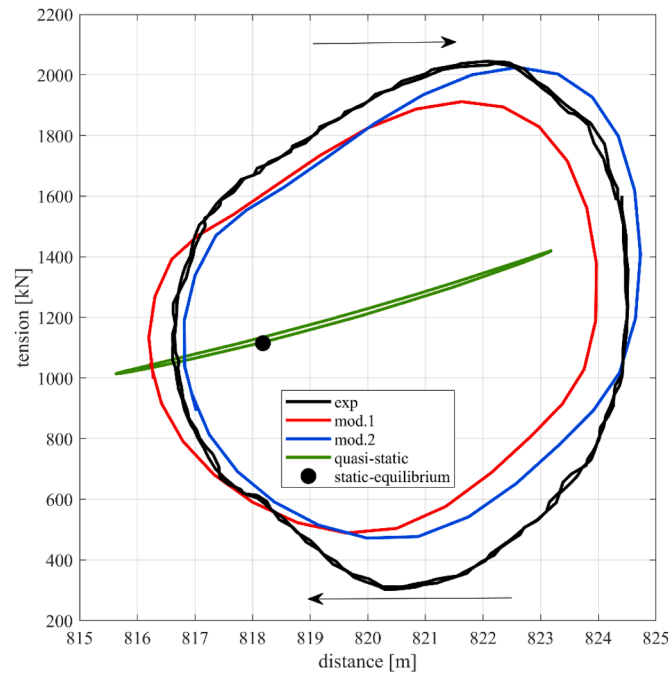**Fig. 8.** DOF[0] responses under extreme regular wave loading

Fig. 9. Motion-tension relation under extreme regular wave loading

where; $C_{p_{ii}}$, $C_{q_{ii}}$ are the diagonal linear and quadratic damping coefficients, respectively, and $\dot{X}_i$ is the structural velocity for translational DOF ($i = 1, 2, 3$) and angular velocity for rotational DOF ($i = 4, 5, 6$).

LC1 decay tests are carried out to calibrate the structure's hydrodynamic linear and quadratic damping. The decrease of motion amplitude, ϕ_n obtained from the decay tests divided by the mean motion amplitude is plotted against the mean motion amplitude as illustrated in Fig. 7 (a). After fitting the data points into a line, the y-intercept of the line, p, and the slope of the line, q, are the values used for calibrating the motion amplitudes in the FDT (Helder and Pietersma, 2013). Fig. 7 (b and c) shows these values post calibrating the model, and the resulting diagonal linear and quadratic damping coefficients are reported in Table 4.

- Mod.2

In addition to the potential solution provided in mod.1 for the large columns, the drag term of Morison's equation is implemented in the second hydrodynamic model called mod.2. Unlike the first model that utilizes still water tests (LC 1), which can lead to highly conservative damping forces due to the absence of waves (Chakrabarti, 1995), making the model erroneously calibrated when tested against wave-induced excitations of various wave heights, wave loading-based calibration method is used in mod.2. The excitation component of the viscous force is calibrated in mod.2 as well. In this calibration method, wave loading cases LC 2 & LC 3 described in Table 3 are utilized instead of LC 1. The horizontal component of the quadratic drag term of Morison's equation serving as non-linear viscous force is calculated at the instantaneous position of the structure. In other words, the relative velocity between the wave-induced water particle velocity, U_i at the ith column, and the structural velocity $\dot{X}$ at the x-y plane is considered. A synthetic coupling parameter μ_c is associated with the hydrodynamic damping-induced velocity to calibrate the structural damping. The drag force (F_{wk}) for a unit depth becomes;

$$F_{wk} = \frac{1}{2}\rho C_{d,\,wk} \sum_{i=1}^{n_{large}} D_i \left(U_i - \mu_c \dot{X}_i \right) \left| U_i - \mu_c \dot{X}_i \right| \tag{13}$$

where; $C_{d,wk}$ is the drag coefficient. The force is then integrated along the spontaneous wetted depth of each column of the semi-submersible, and the total drag force is calculated by summing the contribution from the large columns, n_{large} (upper and base). By assigning a value of unity for the drag coefficient, $C_{d,wk}$, the coupling parameter equals 1.26 when calibrated according to a surge FDT (equivalent to surge quadratic damping coefficient in mod.1). However, it equals a value of 0.25 (80% reduction) when calibrated through the moderate irregular wave case (LC 3). In a similar study, Coulling et al. (2013) validated their model that uses a 90% reduced surge damping coefficient calibrated via FDT. Eq. (13) results in a mean offset in the wave direction. A complementary mean drift force is added so that the overall mean drift viscous-induced force (F_ν) satisfies the following equation (DNV-GL, 2010);

$$F_\nu = \frac{2}{3\pi}\rho g k A^3 C_{d,\,\nu} \sum_{i=1}^{n_p} D_i \tag{14}$$

where; ρ is water density, g is gravitational acceleration, k is the wavenumber, A is the regular wave amplitude or half the significant wave height in case of an irregular wave, n_p is the number of columns piercing the water surface, $C_{d,\nu}$ is the drag coefficient related to the above formula, and D_i is the diameter of the ith column.

Eq. (14) is only applied to the columns above the mean water level to the wave crest (splash zone). The drag coefficient is calibrated according to the mean surge value in the regular moderate load case (LC 2) and is equal to 0.84 for the columns considered.

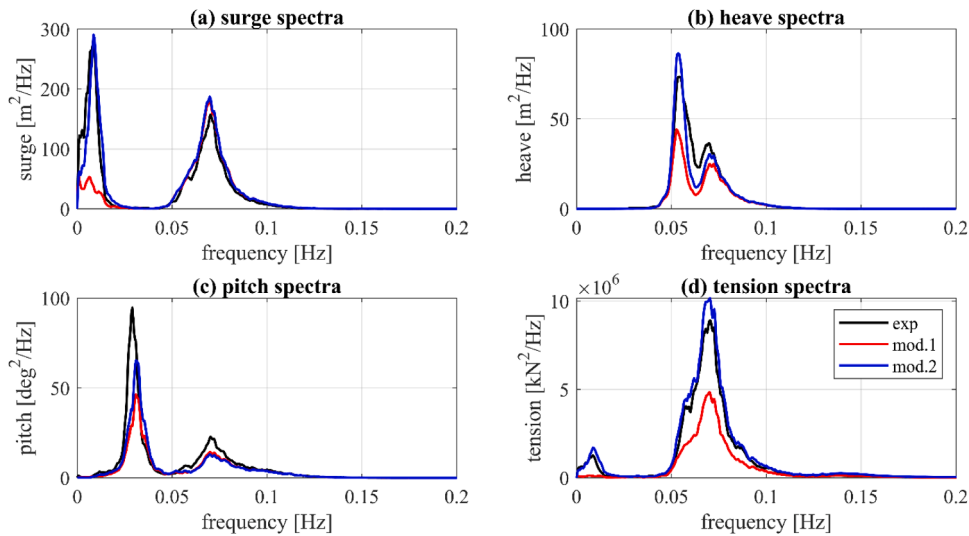To account for the drag force in the z-direction, the bottom surface of

Fig. 10. Frequency-domain comparison of DOF0 under extreme irregular wave excitation
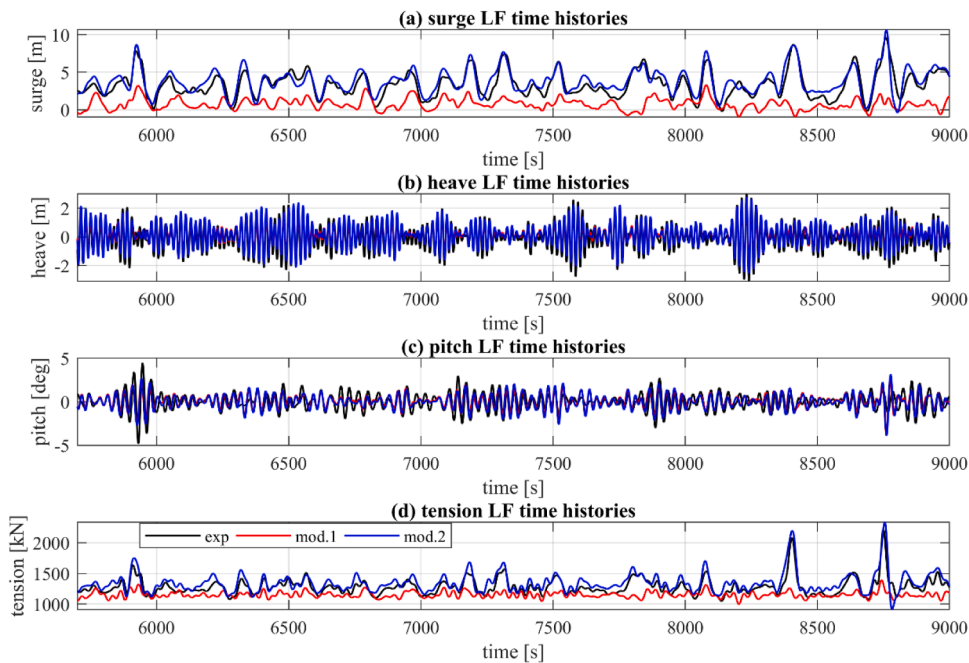

Fig. 11. Low-frequency motion in time-domain for DOF^0 under extreme irregular wave excitation

each of the three base columns and the main column were considered as heave plates. To avoid additional calculations of the inertia forces, the discs' added mass coefficient was set to zero and a value of 4.8 was selected for the normal drag coefficient, C_{dz}, according to the analysis done by Robertson et al. (2014). Table 5 summarizes the selection of the coefficients defining the hydrodynamic properties of each of the calibration schemes in the axial and normal flow directions.

3.2. Validation

The models described above are tested under a total of three load cases: an extreme regular wave (LC 4), an extreme irregular wave (LC 5), and white noise (LC 6). Table 3 provides a brief description of the cases. The mainly excited DOFs under a zero-degree wave incident angle are considered, which are the displacements along the X-direction (surge: X), along the Z-direction (heave: Z), and the rotation around the Y-axis (pitch: RY). Additionally, the tension in the seaward cable (T1) is

considered, as it is the most excited cable among the three catenary mooring lines. These four responses are referred to as (DOF^0).

3.2.1. Extreme regular wave

An extreme regular wave load case is initially employed. Under regular wave and no wind conditions, time-domain results are shown in Fig. 8 for DOF^0. A general agreement with the experimental results is seen for both models.

The relation between tension and structural motions is shown in Fig. 9 demonstrating the fairlead position in time versus cable tension, where arrows show the fairlead excursion's direction. The horizontal axis denotes the shortest distance between fairlead and anchor. As the platform oscillates, the two models' dynamic tensions do not change linearly, and maximum and minimum tension values do not coincide with the greatest or shortest distance but are located close to the furthest position creating a snap-like effect. For the comparison, a quasi-static solution of the mooring cable is also added to Fig. 9. As can be seen
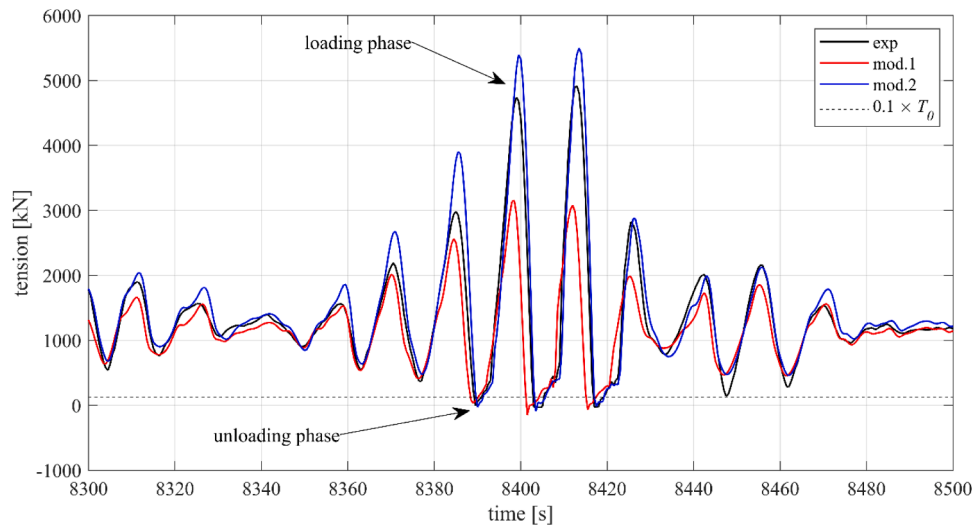
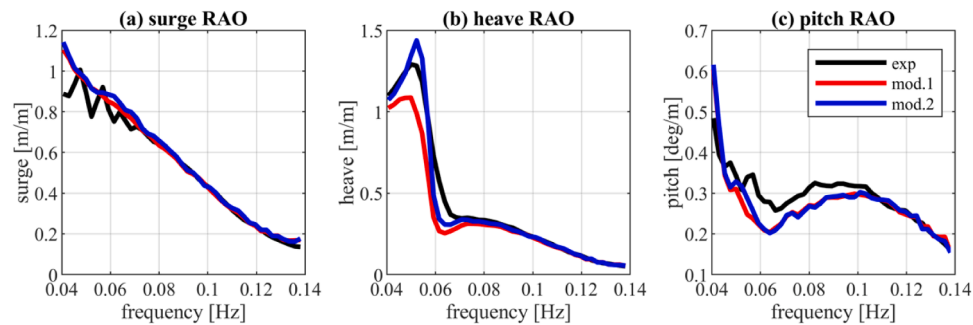**Fig. 12.** Subsequent snap load response occurring in the bow cable T1

Fig. 13. RAO result comparison in surge, heave, and pitch between the experiment and the models under white noise excitation

clearly in Fig..9Figure 9, quasi-static solution does not capture the dynamics of the mooring line. Since mod.2 has a closer mean drift response to the experimental values than mod.1, tension response in mod.2 is enhanced, especially in terms of the maximum tension value. As for the minimum tension, both models have their values higher than that of the experiment.

3.2.2. Extreme irregular wave

For the irregular wave case, the analysis is shifted to the frequency domain. Fig. 10 illustrates the structural response in all models for DOF^0. Both models agree with the experiment in terms of wave-frequency motion response. However, mod.1 suffers from under-predicting the low-frequency responses. In order to analyze the LF responses in detail, they are discerned by applying a low-pass filter with a cutoff frequency f_c corresponding to the lowest power between the LF and WF regions in the spectrum and obtained time series are shown in Fig. 11. The mean drift in surge is 0.8 m for mod.1 and 3.74 m for mod.2, corresponding to 25% and 118% of the experimental value, respectively. Even though the second order potential solution exists in both models, the lack of the exciting component of the viscous drag forces in mod.1 renders it defective to estimate the platform's mean drift motion accurately. While mod.2 is slightly over predicting, it agrees well with the experimental results, proving that inertia and drag effects are more dominant than the diffraction effects for the platform parts.

The slowly varying oscillations are better represented in mod.2 in tension as well. Two models are also compared in terms of capturing the snap loads. A snap load occurs when the cable endures an unloading stage followed by a sudden re-tensioning as shown in Fig. 12. Fig. 12 displays the comparison of the snap load capture of the both models that

was recorded in the experimental study. Note that both models use the dynamic mooring model and can simulate snap load events in the cable tension. However, as can be seen in Fig. 12, the maximum tensions in mod1 are lower than the mod.2 or the experiment in the snap event's loading phase. Therefore, the sole deployment of a dynamic mooring model is not sufficient, and it is just as crucial to correctly model the LF response for accurate readings of the extreme tension values.

A slight under-prediction in pitch is seen for both models. The same pattern is also observed in the regular wave cases as given in Fig. 8. Overall, despite being calibrated according to the moderate case, mod.2 preserves its accuracy under extreme conditions, emphasizing the wave-based calibration model's applicability under various environmental conditions. The same cannot be stated if one takes free decay tests as the sole source of calibration as the system's damping properties are dependent upon the extremity of the loading (Gueydon, Duarte, and Jonkman, 2014). Mod.2, on the other hand, is advantageous since the water particle velocity and the mean drift viscous force are functions of wave height.

3.2.3. White noise

Lastly, primary responses are compared against the experiment under white noise excitation using response amplitude operators (RAO). A general agreement is observed, and the difference between the two models is mostly minute, as Fig. 13 shows. The models' under prediction of the pitch response explains the discrepancies previously presented at the WF response for this DOF. Heave in LF is greatly enhanced in mod.2.
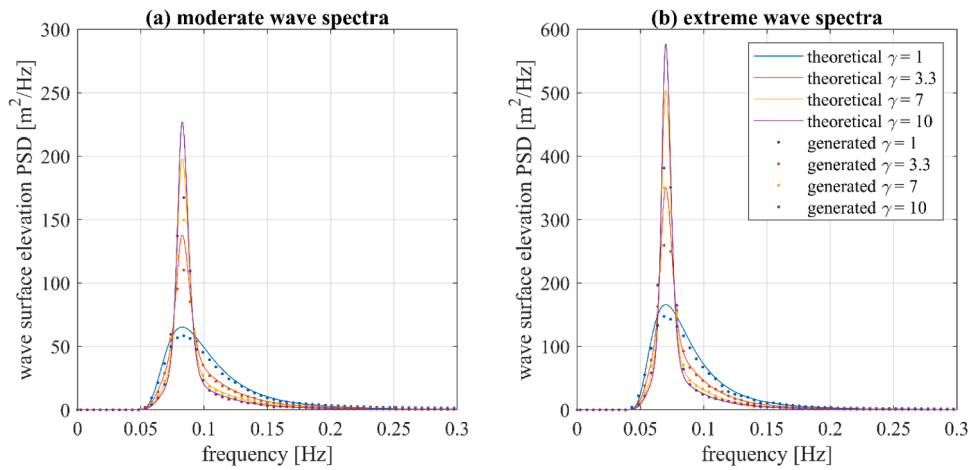
Fig. 14. Power spectral density for the theoretical and the generated wave surface elevation
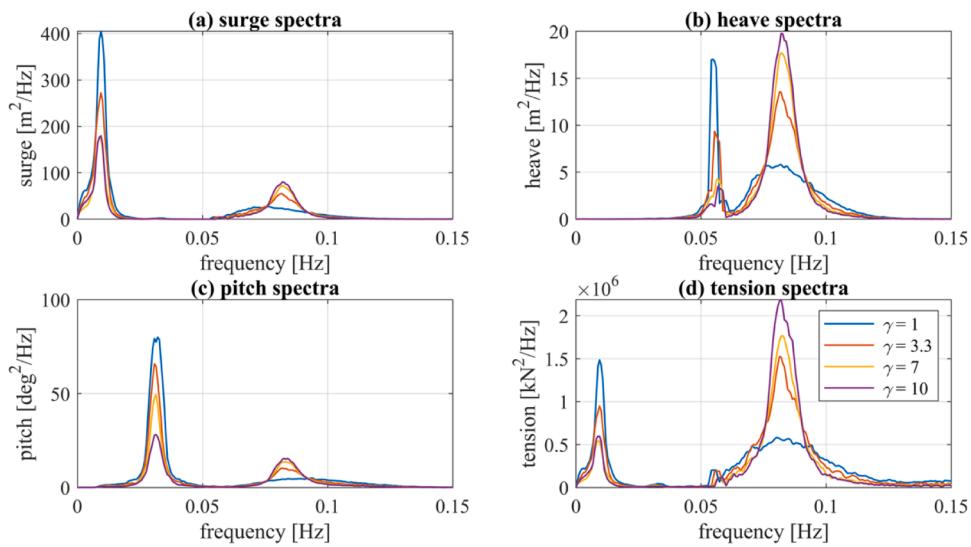
Fig. 15. PSD results for the influence of the spectrum shape on the main responses for the moderate wave case
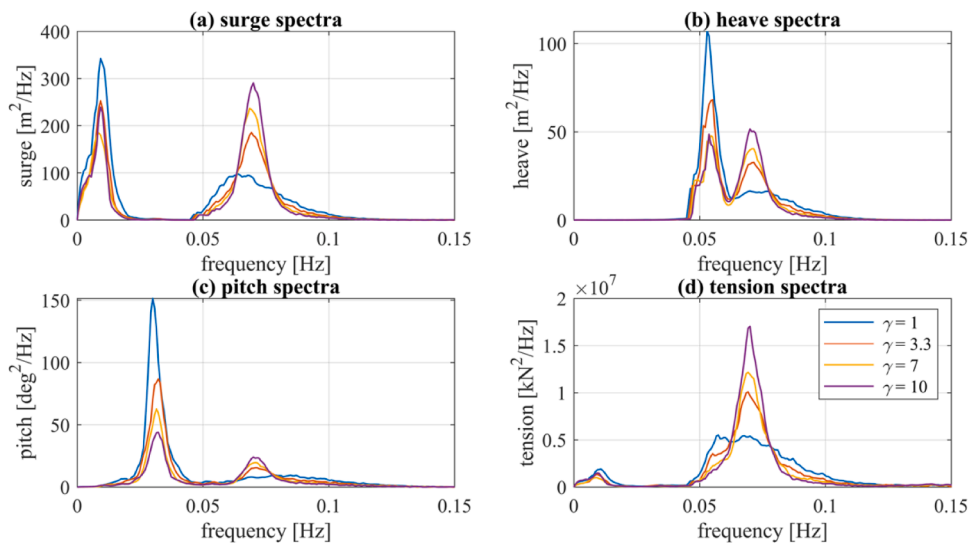
Fig. 16. PSD results for the influence of the spectrum shape on the main responses for the extreme wave case
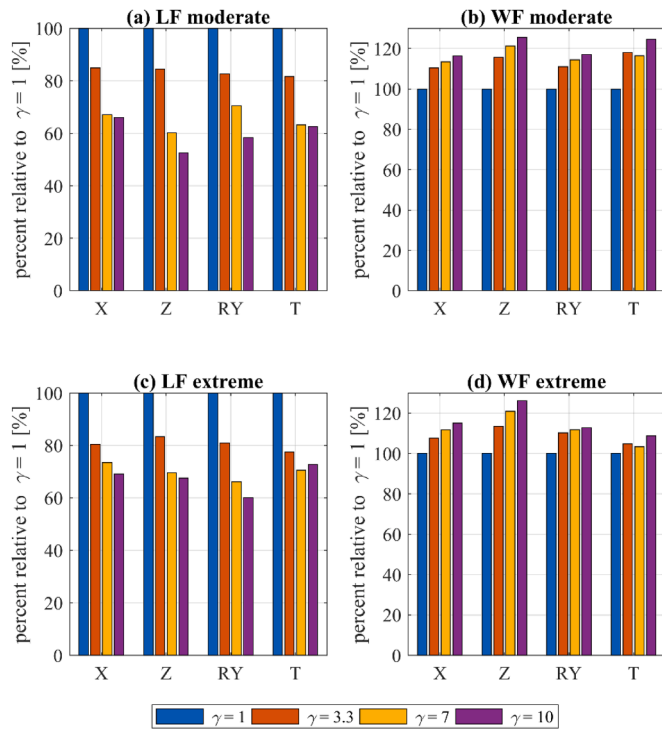
Fig. 17. Percent change of LF and WF response amplitudes in different spectral shape cases relative to the amplitude in the spectrum case with $\gamma = 1.0$ (PM)

Table 6
synthetic wave spectrum settings for testing wave irregularity effects

Spectrum Case	γ	ν	H_{10}/H_s
I	1.0	0.39	1.23
II	3.3	0.33	1.25
III	7.0	0.28	1.26
IV	10.0	0.26	1.27

4. Effect of Wave Irregularity on the Structural Response

Irregularity is an essential feature of sea waves. The frequency spectrum, which is the wave energy distribution in frequency, and the directional spreading of the wave energy are the known representations of the wave irregularity. In this study, after validating mod.2, the effects of frequency spectrum shape and multi-directional waves on the floating wind turbines' response are investigated in LF and WF regions.

4.1. Effect of frequency spectrum shape

The distribution of wave energy over the frequency is represented by the frequency spectrum $S(f)$. The frequency spectrum model for sea waves can be formulated as follows (Ozbahceci et al. 2002):

$$S(f) = \beta H_{1/3}^2 T_p^{(1-m)} f^{-m} \exp\left[-(m/4)\left(T_p f\right)^{-4}\right] \gamma^{\exp\left[-\frac{(T_p f - 1)^2}{2\sigma^2}\right]} \quad (15)$$

where; γ is the peak enhancement factor, f_p the peak frequency, $T_p = 1/f_p$, m, is the coefficient which determines the high frequency slope of the spectrum, and:

$$\beta \cong \begin{cases} \dfrac{0.0624 m^{(m-1)/4}}{4^{(m-5)/4}\Gamma[(m-1)/4]}\left[1 + 0.7458(m+2)^{-1.057}\right] & if \; \gamma = 1 \\[2ex] \dfrac{0.0624 \; (1.094 - 0.01915\ln\gamma)}{0.230 + 0.0336\,\gamma - 0.185(1.9 + \gamma)^{-1}} & if \; \gamma > 1 \end{cases} \quad (16)$$

$$\sigma \cong \begin{cases} 0.07 \; : \; f \le f_p, \\ 0.09 \; : \; f > f_p. \end{cases} \quad (17)$$

When the peak enhancement factor, γ is equal to 1.0, and the coefficient for the high-frequency slope, $m = -5$, Eq. (15) gives the well-known Pierson-Moskowitz (PM) spectrum for fully developed wind waves. When $\gamma = 1.0$ and the coefficient for the high frequency slope, m is different than -5 in Eq. (15), it is Wallops spectrum proposed by Huang to obtain a spectrum with a high frequency tail attenuating rapidly or gradually compared to the PM spectrum (Goda, 2010). The storm waves generated by strong winds in a relatively small sea area feature concentrated wave energy in a narrow frequency range, i.e., the frequency spectrum exhibits a sharp peak. This feature was examined in detail by the Joint Wave Observation Project in the North Sea (JONS-WAP). The result of spectral measurements was compiled in the form of modification to the Pierson-Moskowitz spectrum by enhancing the spectral peak, as Hasselmann et al. (1973) reported. The resultant spectral function is called the JONSWAP spectrum after the name of the project. The original expression included the wind speed as the parameter, but it has been rewritten by Goda (2010) with the significant wave height, H_s, and spectral peak period, T_p. When the peak enhancement factor, γ is higher than 1.0 and the coefficient for the high frequency slope, $m = -5$, Eq. (15) gives JONSWAP spectrum. Hasselmann et al. (1973) reported the peak enhancement factor γ varying between 1 and 7 with a mean of 3.3. Eq. (15) can also represent the swell spectrum by setting $\gamma = 7$ to 15, as indicated by Goda (2010) in his analysis of the swell traveling over a distance of 7000 to 9000 km.

In this study, to get a wave energy spectrum in different shapes, the peak enhancement parameter, γ in Eq. (15) is changed. Four spectral shapes are used since they may represent the spectral shape in the application range from broad to narrow and sharp. 3-hours-long time series are created synthetically using DSA (Deterministic Spectral Amplitude) method by keeping the significant wave height H_s, peak period T_p and the coefficient m constant but changing peak enhancement factor, γ as 1 (PM spectrum), 3.3, 7, and 10. The agreement between the theoretical and generated spectra is depicted in Fig. 14.

The constant parameters of the moderate and extreme wave load cases given in Table 3 (LC 3 and LC 5, respectively) are used to examine the influence of spectrum shape upon the LF and WF responses of the structure, while the extreme case is also analyzed for the mooring

Table 7
frequency- and time-domain wave statistics comparison between a uni-directional case and multi-directional cases

		frequency-domain		time-domain					
		H_{m_0}(m)	f_p(Hz)	$H_{1/10}$(m)	$H_{1/3}$(m)	H_{mean}(m)	$T_{1/10}$(s)	$T_{1/3}$(s)	T_{mean}(s)
uni-directional	–	10.49	14.17	12.59	10.01	6.28	16.59	14.91	11.14
multi-directional	$n = 2$	10.49	14.17	12.08	9.72	6.18	15.30	13.37	9.74
	$n = 4$	10.49	14.17	12.06	9.69	6.13	15.36	13.53	9.75
	$n = 6$	10.49	14.17	12.11	9.73	6.15	15.43	13.57	9.78
	$n = 20$	10.49	14.17	12.29	9.80	6.19	15.41	13.56	9.78
	$n = 200$	10.49	14.17	13.81	10.27	6.35	15.38	13.54	9.78

Fig. 18. wave grouping factor, mrl of each spectrum shape for (a) moderate and (b) extreme wave case
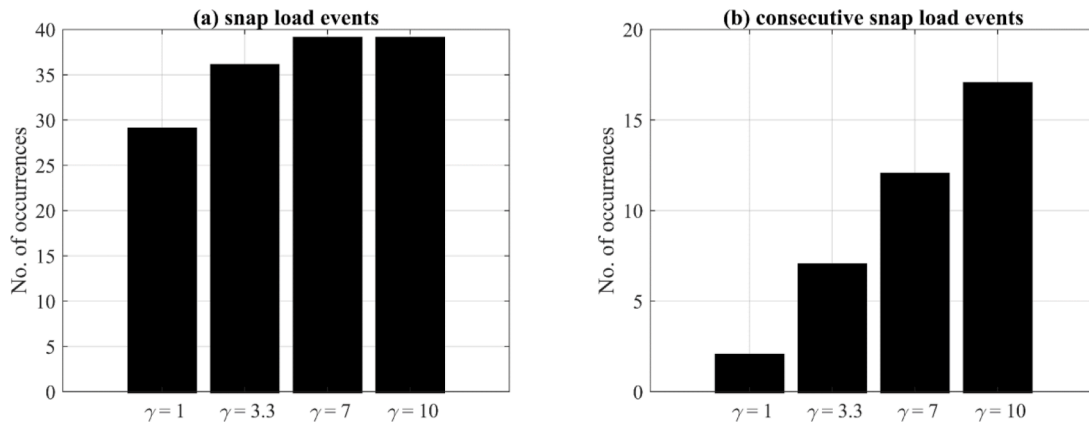
Fig. 19. (a) Snap load occurrences in the most loaded cable (T1) under the extreme waves with different γ values b) mean successive snapping loads in the T1 cable under extreme waves of different γ values
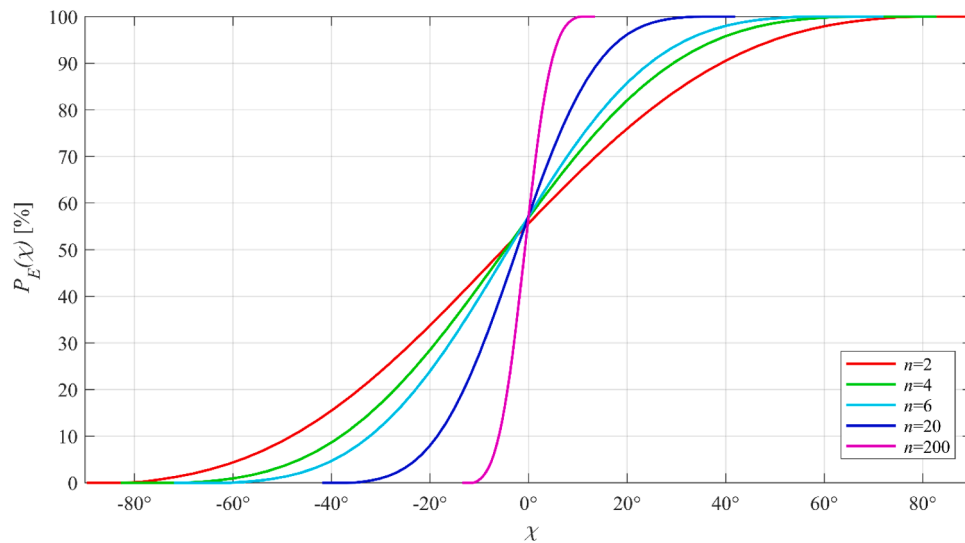
Fig. 20. directional distribution of energy for the various spreading parameters

tensions and snap load events. Since uni-directional waves with the incidence angle of zero degree are used in the simulations, power spectral densities (PSD) for surge (X), heave (Z), pitch (RY), and tension in T1 (T) corresponding to four different spectral shapes are compared in Fig. 15 and Fig. 16 for the moderate and extreme cases, respectively. The PSD values at the LF region in both loading cases seem to reduce in their
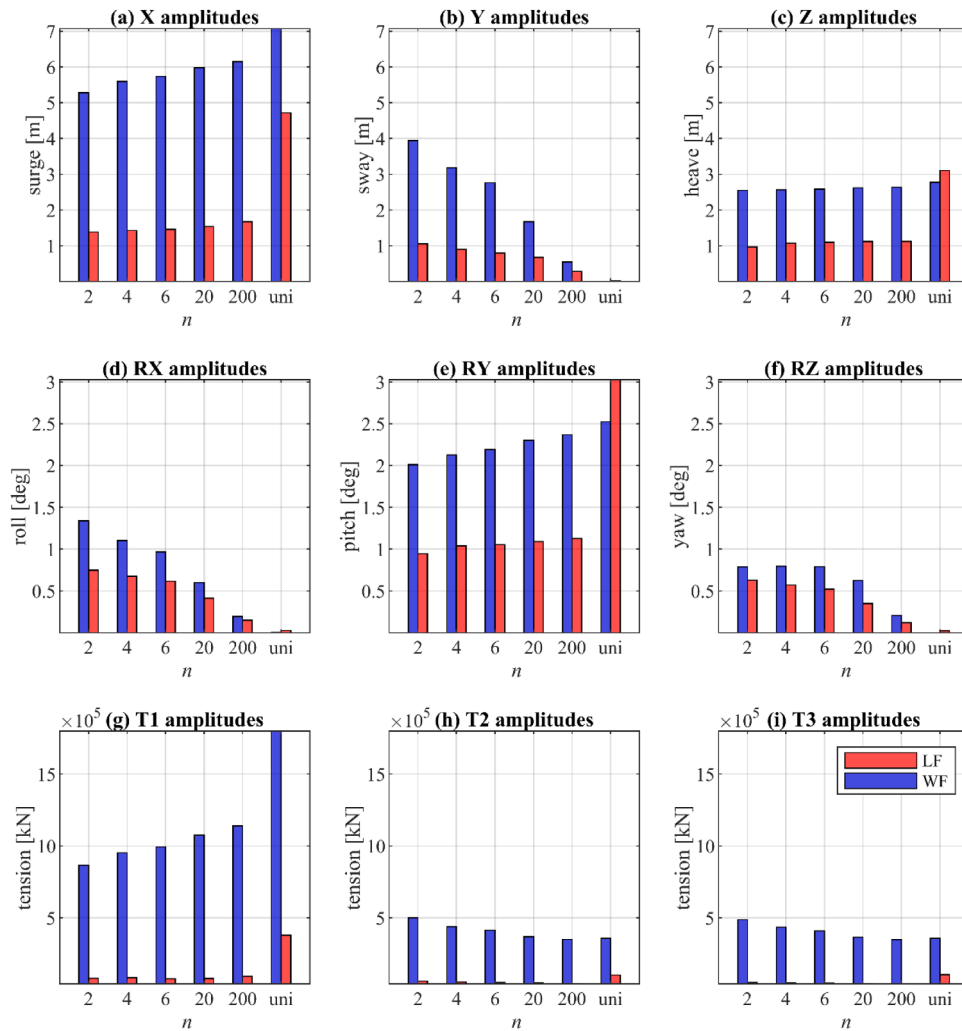
Fig. 21. structural motion and cable tensions showing the gradual change between a uni-directional and a multi-directional excitation

Table 8
snap load events as a function of the spreading of the wave

	Multi-directionality Spreading parameter (n)					Uni-directionality
	2	4	6	20	200	
Snap load occurrence	0	0	0	0	1	29

peakedness as the γ increases while WF responses tend to reach higher points with an increase in the peak enhancement factor. In order to make a numerical comparison, the values of LF and WF responses are represented by their amplitudes, A_{LF} and A_{WF} derived from the corresponding spectrum, $S(f)$ as follows:

$$A_{LF} = 4\sqrt{\int_0^{f_c} S(f)df}, \quad A_{WF} = 4\sqrt{\int_{f_c}^{cf_p} S(f)df}, \quad j = 1, 2, \ldots 4 \tag{18}$$

where; f_c is the cutoff frequency separating the LF and WF excitations in the spectrum. To avoid irregularities in the high frequency, c is chosen as 1.3.

Percent changes of LF and WF amplitudes in different spectral shape cases relative to the response amplitudes in PM spectrum case ($\gamma = 1.0$) are given in Fig. 17. Fig. 17 demonstrates that the change in the response amplitudes due the higher γ values is similar in the moderate and extreme cases. Therefore, results obtained in the comparative study are independent from the wave period and the wave height but they should be in a range that can excite the structure motion. Regardless of the extremity of the wave, changes in the spectral peakedness have a more prominent effect on LF than on WF regions. The reduction of LF is around 20% for $\gamma = 3.3$ and goes up to 40% for $\gamma = 10$. The corresponding percentage increase in WF are around 10% and 30%, respectively.

The direct correlation between WF responses and γ values may be the narrowness of the spectral shape (the concentration of energy into a smaller wave frequency bandwidth) that may affect the distribution of wave heights and wave grouping. The narrowness of the spectral shape can be determined by Longuet Higgins's parameter (ν). It is defined as follows:

$$\nu^2 = \left(m_0 m_2 - m_1^2\right)/m_1^2 \tag{19}$$

where;

$$m_n = \int_0^{\infty} f^n S(f)df \tag{20}$$

The parameter takes the value between 0 and 1, and the closer it is to zero, the narrower the spectrum becomes. As shown in Table 5 and in Fig. 14, the spectral shape becomes narrower and sharper from spectrum I to IV.

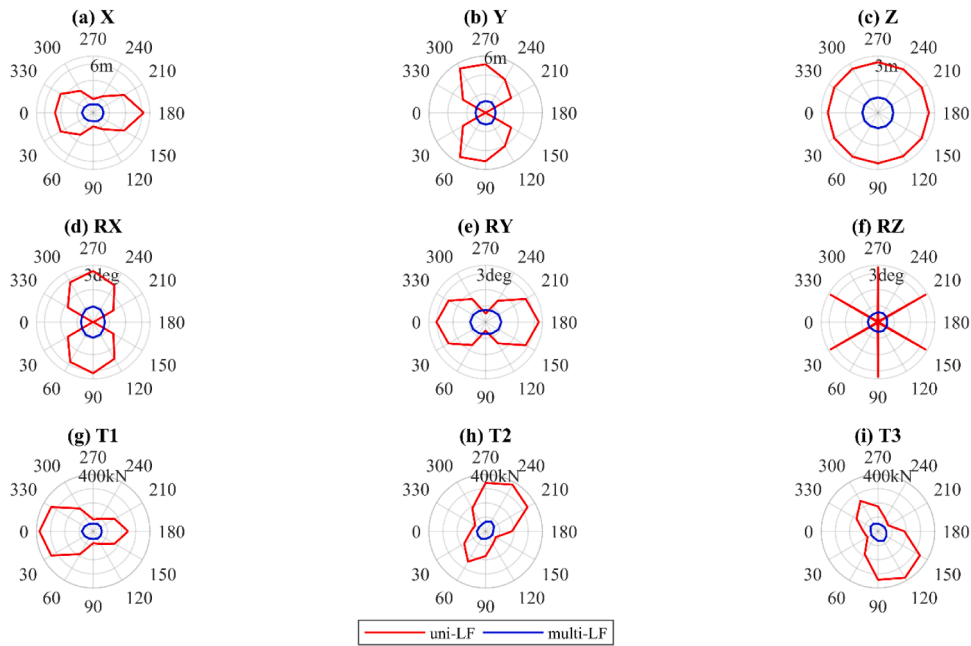Individual wave heights of actual ocean waves are known to follow

Fig. 22. LF responses for both uni-directional and multi-directional wave excitation. The radii are the amplitudes A_{LF}.
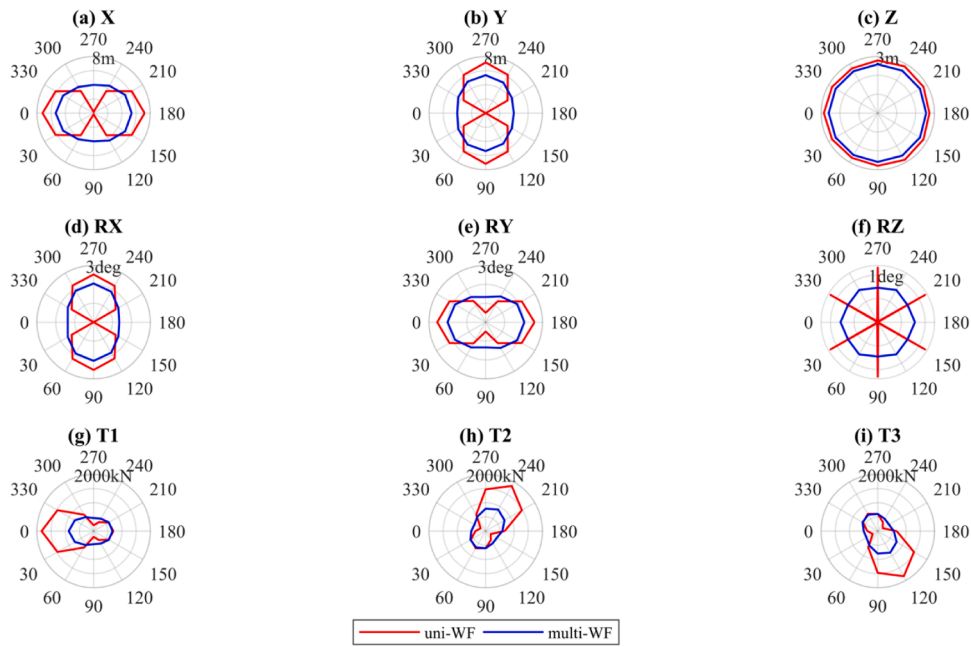

Fig. 23. WF responses for both uni-directional and multi-directional wave excitations. The radii are the amplitudes A_{WF}.

the Rayleigh distribution approximately. According to Rayleigh distribution derived based on the narrow spectrum, the ratio $H_{10}/H_s = 1.27$. H_{10} is the mean of the greatest one-tenth wave heights in the wave profile. The ratio of H_{10}/H_s can be used to check the deviation of wave height distribution from the Rayleigh. H_{10}/H_s values corresponding to four spectral shapes are given in Table 6, which shows when the spectrum becomes narrower, H_{10}/H_s ratio increases.

Therefore, it can be stated that the reason behind the change in the structural response in WF and LF is due to the concentration of energy into a smaller wave frequency bandwidth and an increase in the higher waves in an irregular time series as the spectrum becomes narrower.

Another spectrum shape effect may be the wave grouping. A basic definition for wave grouping can be given as the sequence of high waves

in a wave train. Up to now, many parameters and different methodologies have been used to characterize wave groups. In this study, the mean run length defined by Goda (2010) is used to check the wave grouping. The *run length* is the number of waves exceeding a specified value of the wave height H_c (the mean wave height $\overline{H}$ in this study) without falling below that height. A succession of such high waves is called a *run* of high wave heights. *Mean run length* (*mrl*) is the sum of run lengths divided by the number of runs in a wave series. *mrl* for the four cases given in Table 7 are calculated for both moderate and extreme wave cases. Frequency spectra and the calculated *mrl* values are shown in Fig. 18. It should be noted that the difference in the significant wave height is less than 5% in the time series corresponding to the given four spectral shapes. The figure shows that grouping in the wave train is

Table 9

Under-over prediction comparison between uni-directional/multi-directional excitation-induced response amplitudes

direction (deg)	low-frequency									wave-frequency								
	X	Y	Z	RX	RY	RZ	T1	T2	T3	X	Y	Z	RX	RY	RZ	T1	T2	T3
0	U	M	U	M	U	M	U	U	U	U	M	U	M	U	M	U	M	M
30	U	U	U	U	U	U	U	U	U	U	M	U	M	U	U	U	M	M
60	U	U	U	U	U	M	U	U	U	M	U	U	U	M	M	U	U	U
90	U	U	U	U	M	M	U	U	U	M	U	U	U	M	M	M	M	U
120	U	U	U	U	U	M	U	U	U	M	U	U	U	M	M	M	M	U
150	U	U	U	U	U	U	U	U	U	U	M	U	M	U	U	M	M	U
180	U	M	U	M	U	M	U	U	U	U	M	U	M	U	M	U	U	U
210	U	U	U	U	U	U	U	U	U	U	M	U	M	U	U	M	U	M
240	U	U	U	U	U	M	U	U	U	M	U	U	U	M	M	M	U	M
270	U	U	U	U	M	U	U	U	U	M	U	U	U	M	U	M	U	M
300	U	U	U	U	U	M	U	U	U	M	U	U	U	M	M	U	U	U
330	U	U	U	U	U	U	U	U	U	U	M	U	M	U	U	U	M	M
U	uni-directional > multi-directional																	
M	uni-directional < multi-directional																	

Table 10

LF-WF comparison between uni-directional/multi-directional excitation-induced response amplitudes

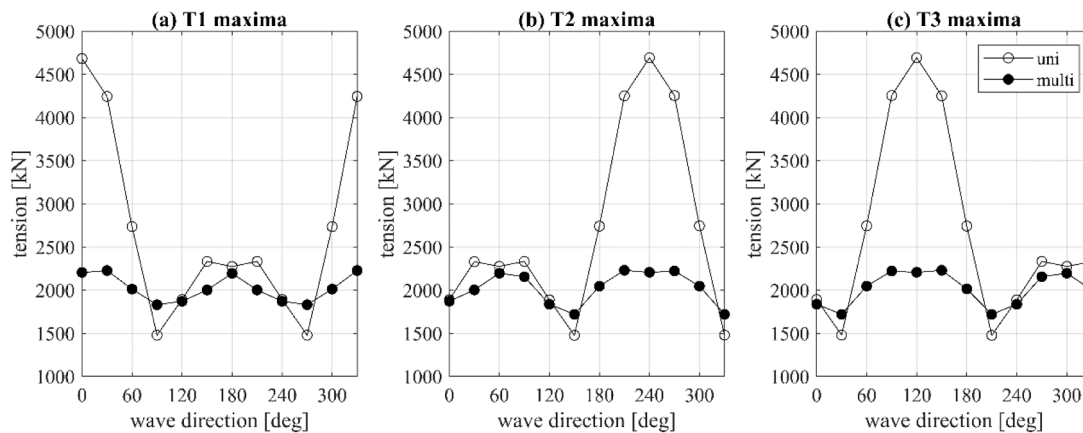| direction (deg)	uni-directional									multi-directional								
	X	Y	Z	RX	RY	RZ	T1	T2	T3	X	Y	Z	RX	RY	RZ	T1	T2	T3
0	W	L	L	L	L	L	W	W	W	W	W	W	W	W	W	W	W	W
30	W	W	L	L	L	L	W	W	W	W	W	W	W	W	W	W	W	W
60	W	W	L	L	L	L	W	W	W	W	W	W	W	W	W	W	W	W
90	W	W	L	L	L	L	W	W	W	W	W	W	W	W	W	W	W	W
120	W	W	L	L	L	L	W	W	W	W	W	W	W	W	W	W	W	W
150	W	W	L	L	L	L	W	W	W	W	W	W	W	W	W	W	W	W
180	W	L	L	L	L	L	W	W	W	W	W	W	W	W	W	W	W	W
210	W	W	L	L	L	L	W	W	W	W	W	W	W	W	W	W	W	W
240	W	W	L	L	L	L	W	W	W	W	W	W	W	W	W	W	W	W
270	L	W	L	L	L	L	W	W	W	W	W	W	W	W	W	W	W	W
300	W	W	L	L	L	L	W	W	W	W	W	W	W	W	W	W	W	W
330	W	W	L	L	L	L	W	W	W	W	W	W	W	W	W	W	W	W
L	low-frequency > wave-frequency																	
W	low-frequency < wave-frequency																	
U	uni-directional > multi-directional																	
M	uni-directional < multi-directional																	

Fig. 24. tension maxima in uni- and multi-directional excitations

pronounced as the wave spectrum becomes narrower as anticipated (Longuet-Higgins 1957, Ozbahceci et al. (2002)).

The effect of the frequency spectrum shape on the mooring lines is also investigated in terms of snap loads. The identification methodology of a snap load is the same as the one reported in Hsu et al. (2017). Briefly, it is based on the definition that a snap load is said to occur whenever the dynamic tension falls 90% below the static tension (unloading phase) and is succeeded with a sudden re-tensioning of the

cable (loading phase) (DNV-GL 2011). Applying this minimum-based criterion into the zero-up-crossed tension response in the extreme condition gives the number of snap loads delineated in Fig. 19 (a). Snap loads occur 25% more when γ changes from 1 to 3.3. Successiveness in such fatigue loads is severely hazardous. A successive snap load event occurs whenever the upper criterion is triggered consecutively, and the number of repeated snap loads in such an event is averaged throughout the time series and represented in Fig. 19 (b). As γ rises, snap events

Table 11
snap load occurrences in uni-directional loading at various wave direction

| | Wave direction (deg) | | | | | | |
	0	30 or 330	60 or 300	90 or 270	120 or 240	150 or 210	180
	Uni-directional						
mooring line	T1	T1	-	T3/T2	T3/T2	T3/T2	-
Snap load occurrence	29	13	-	13	29	13	-
	Multi-directional						
mooring line	-	-	-	-	-	-	-
Snap load occurrence	-	-	-	-	-	-	-

alternate from being sporadically distributed throughout the time series to a more successive nature due to the wave grouping effect being more pronounced in higher γ.

4.2. Effect of directional spreading for various wave angles

The spectrum of natural sea waves is a function of both frequency and direction $S(\omega,\chi)$:

$$S(\omega,\chi) = G(\omega,\chi)S(\omega) \tag{21}$$

where; $G(\omega, \chi)$ is the nth-powered cosine directional spreading function and can be defined as follows:

$$C\cos^n\left[\frac{\pi}{\Delta\chi}(\chi-\overline{\chi})\right] \; for \; -\frac{\Delta\chi}{2} < \chi < \frac{\Delta\chi}{2} \tag{22}$$

where; n represents the spreading parameter, $\overline{\chi}(\omega)$ is the mean wave direction for each frequency. The constant C is chosen to satisfy that the total energy in both the multi-directional and the uni-directional spectrum is equal. Therefore:

$$\int_{-\frac{\Delta\chi}{2}}^{\frac{\Delta\chi}{2}} G(\omega,\chi)\cdot d\chi = C\int_{-\frac{\Delta\chi}{2}}^{\frac{\Delta\chi}{2}} \cos^n\left[\frac{\pi}{\Delta\chi}\chi\right]\cdot d\chi = 1 \tag{23}$$

4.2.1. Effect of directional spreading on the FOWT responses

To explore the change in the response under various levels of directional wave spreading, the directional spectra having five spreading parameter values were examined: 2, 4, 6, 20, and 200 and

compared with the standard, uni-directional case. Fig. 20 reveals the cumulative energy distribution among the different multi-directional spectra. The other wave parameters are identical to LC 5. As the spreading parameter increases, the directional range shrinks, and the energy becomes more concentrated around the main direction.

To insure fair comparison, Table 7 outlines the agreement of the wave statistics at the point of origin in both frequency-domain and time-domain for uni-directional and multi-directional wave profile. In order to better estimate second order excitations, the validated mod.2 approach is used after multi-directional adaptation. The model is applied to calculate the forces originating from the individually weighted sub-spectra and use superposition to find the total longitudinal and lateral forces exerted on the platform.

The resulting motion corresponding to different directional spreading is separated into LF and WF amplitudes calculated by applying Eq. (16)Eq. 18 with $c = \infty$. The amplitudes are illustrated in Fig. 21, together with the uni-directional case results. Uni-directional means that there is no directional spreading and n goes to infinity. Multi-directional sea state always produces lower low-frequency motion compared to uni-directional one. As for the wave-frequency component, the platform responds similarly in the heave direction. However, as the wave becomes less multi-directional, lateral responses (sway Y, roll RX, and yaw Z) approaches zero due to the directional shrink, while the longitudinal responses (surge X, pitch RY, and bow cable tension T1) increase in value and gets closer to their uni-directional counterparts. But a multi-directional setting of the highest spreading parameter ($n = 200$) does not create the same excitation as the uni-directional case due to the singularity effect produced where the uni-directional spectrum's weight is equal to one for solely one direction. This proves that uni-directional assumptions can be unrealistically conservative in primary responses (here, surge and tension in T1). Subsequently, this conservatism has a high impact on the number of snap load events provided in Table 8. The uni-directional loading triggers 29 snap events on the most loaded cable T1, while the case with $n = 200$, which is the closest-to-uni-directional loading, causes one snap event and none for spectra with higher spreading values. Note that there is a slight difference between the amplitude values of uni-directional results in Fig. 21 and the ones presented in Fig. 10 since the wave profiles are different. The wave surface elevation is synthetically produced here, while previously, the measured wave elevation from the experiment is used.
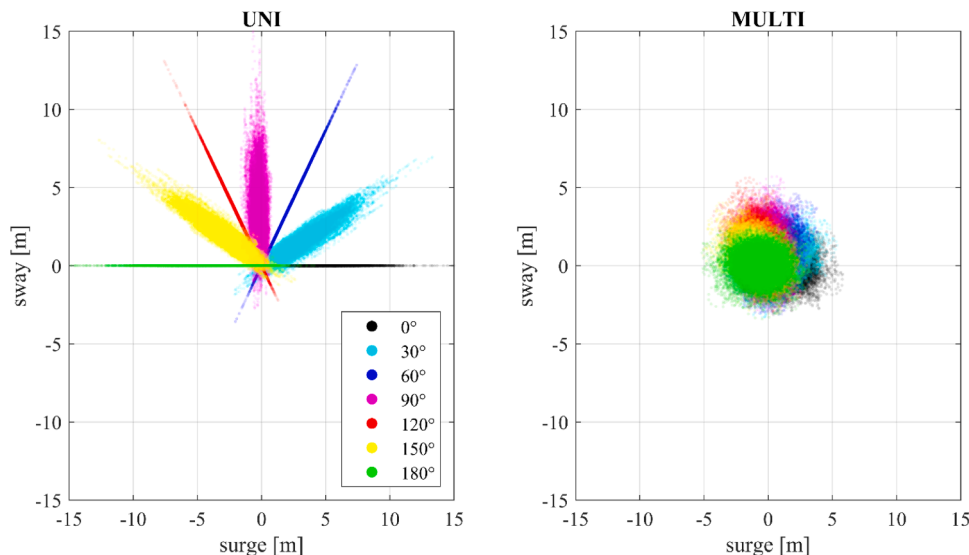

Fig. 25. Surge. vs. sway excitations at different wave direction

4.2.2. Uni-directional vs. multi-directional excitations for a various angle of attacks

In this study, sensitivity analysis of the semi-submersible platform response in all DOF and all cable tensions to wave direction is performed for uni-directional and multi-directional waves while keeping other parameters such as the significant wave height and the peak period constant. The mean direction $\bar{\chi}$ ranges from 0 degree (aligned with the same direction as the seaward mooring T1) to 180 degree (aligned opposite to the seaward mooring T1, See Fig. 2) in intervals of 30 degree. The spreading parameter is set to $n = 2$, the total spreading angle for each multi-directional loading is 180 degree, and the number of sub-spectra in the total multi-directional spectrum is set to 27. The PSD of each sub-spectrum is evaluated at 200 frequency points. To preserve the system's symmetry, the wind turbine always has to face the wave's main direction to ensure identically distributed mass among the tests.

Results are replicated for the remaining directions (ranges from 180 to 330 degree) due to the submerged portion of the platform being geometrically symmetric in the xz-plane (see Fig. 2). Fig. 22 and Fig. 23 are the illustrations under a uni-directional and multi-directional wave excitation from all angles of attack for LF and WF amplitudes, respectively.

Fig. 21 and Fig. 22 show that multi-directional amplitudes are generally less susceptible to variance in direction. For instance, as uni-directional surge and pitch take an ∞-like shape, sway and roll take an 8-like shape in the wave-frequency, multi-directional response takes an elliptic form. Heave amplitude does not alter with direction rendering it utterly transparent to where the wave is coming from and its WF component to whether the loading is uni- or multi-directional. Similar transparency is also observed in the WF response of multi-directional yaw. Additionally, LF responses are notably less symmetric than WF. Tension responses are asymmetric. They inflate when the wave is aligned with the cable due to the wave-induced mean drift effect. The inflation range is ± 30 degrees and is more apparent in uni-directional events. This effects the horizontal excursion of the paltform. T1, for example, allows a more slowly varying surge to be produced when the wave hits the platform's backside (180 degree) than when it is aligned with it (0 degree).

Both Fig. 22 and Fig. 23 are summarized in Table 9 in terms of which loading leads to relatively higher responses. As far as low-frequencies are concerned, the uni-directional assumption is highly conservative (90% of the time), especially mooring tensions. Meanwhile, in wave-frequencies, multi-directional has higher results in almost 40% of cases. In WF, uni-directional normally over-predicts axial responses (surge & pitch in 0 ± 30 deg, 180 ± 30 deg; sway & roll in 90 ± 30 deg, 270 ± 30 deg), similar to the results of previous studies (Zhang and Ishihara 2016; Waals 2009). This pattern reverses for lateral responses (sway & roll in 0 ± 30 deg, 180 ± 30 deg; surge & pitch in 90 ± 30 deg, 270 ± 30 deg). Therefore, concluding uni-directional being consistently conservative is not quite veracious. Multi-directional yaw is seen higher than that excited by a uni-directional load when the wave is aligned with any of the offset columns (0, 60, 120, 180, 240, and 300 degree). However, multi-directional yaw in the low-frequency region is slight compared to misaligned uni-directional, low-frequency yaw.

Table 10 summarizes the results when comparing LF with WF amplitudes. WF responses dominates in most of the cases. However, in the uni-directional case, heave and all rotational responses have a higher LF component. It is common to observe that a WF response ensures a LF response in the same direction. Nevertheless, it is noteworthy to underline that for some cases, despite the absence of a WF motion in a given direction, the structure can still oscillate at low frequencies in that direction. One example is the uni-directional wave with 90 and 270 degree angles. The wave generates WF fluctuations in sway but not in the surge direction. However, the sway motion creates restorations in the surge direction due to the particular mooring configuration of the OC5 semi-submersible FOWT, leading to LF surge motions. The opposite pattern is seen in sway.

Due to the spreading effect of multi-directional excitation, cable tensions are not as extreme as in the uni-directional case. Fig. 24 delineates tension maxima with respect to angle of attack. Multi-directional maxima are observed to be higher than their uni-directional counterparts when the wave is perpendicular to the cable allignment plane.

Snap loads in the mooring cables under uni-directional and multi-directional waves are also investigated. Although snap loads do occur in uni-directional loading, they are absent when the wave energy is distributed over a wide range of directions. Table 11 summarizes the number of snap load occurrences and the mooring line that snap load is detected. It is noteworthy to mention that snap loads do not occur in the directions opposite to the cable (60, 300, and 180 degree) because the wave induces the platform to drift toward the cable reducing the fairlead-anchor distance. Under a 30° of misalignment, cables experience less than half the number of snap loads when excited by a uni-directional loading compared to an alignment case. These findings are supported by Fig. 25, which illustrates the platform's horizontal translations for both uni-directional and multi-directional excitations at the designated directions. The energy is concentrated the most when the surge-sway response shows a straight line, and for this reason, snap load events occur. The energy is well dispersed in the multi-directional incident that the platform does not abruptly cause snap-inducing motions.

5. Conclusions

A numerical investigation of DeepCwind semi-submersible floating wind turbines is carried out, and two hydrodynamic calibrating methodologies have been investigated. The free decay test-based calibration showed a lower response in the low-frequency range. On the other hand, the more dynamic calibration that considers drag term in Morison's equation and a mean drift viscous force enhanced the LF region's results.

Wave irregularities impact on the system is also highlighted by testing similar energetic wave fields with distinctive wave spectra shape characteristics. The direct correlation of narrower spectra with wave-induced motion and its inverse correlation with low-frequency motion is deduced. Snap load events are more likely to occur, and its successiveness grows with a highly grouped wave train, which is pronounced as the wave spectrum becomes narrower. The frequent sudden loading and unloading in the mooring lines are perilous as it drastically reduces the lifespan of the cables.

Another aspect of analyzing irregularity influence on the platform's motion is by studying the variations induced by waves coming from different directions and the directional spreading of these waves. When comparing a uni-directional wave with various directionally spread waves, it is observed that the resulting responses under uni-directional waves are over-predictive. However, concluding that uni-directional assumption always results in overly predicted outcome is spurious as some DOF are not energized by a wave coming from the axial direction. The condition of a multi-directional-induced motion being higher than the conventional uni-directional loading has appeared in multiple cases, especially in the wave-frequency region, although it does not lead to excessive responses like the uni-directional wave. The variation of LF and WF motion with different directions is not always correlated. Surge and tension slowly vary even though wave excitation might be absent in that direction. A general pattern of similarity between 60 and 120 degree and dissimilarity between 0 and 90 degrees is observed. It is also concluded that heave seems transparent of the wave directionality and the spreading of the wave. Snap loading is a function of wave alignment with the cable.

Author statement

All authors have seen and approved the final version of the manuscript being submitted. They warrant that the article is the authors'

original work, hasn't received prior publication and isn't under consideration for publication elsewhere.

Dr. Berguzar Ozbahceci

Yuksel Ruwad Alkarem

Declaration of Competing Interest

No.

Acknowledgement

References

Abou-Rayan, A.M., Khalil, N.N., Afify, M.S., 2016. Dynamic behavior of TLP's supporting 5-MW wind turbines under multi-directional waves. Ocean Systems Engineering 6 (2), 203–216. https://doi.org/10.12989/ose.2016.6.2.203.

Inc, ANSYS, 2013. Aqwa Theory Manual, 174.

Archer, C.L., Jacobson, M.Z., 2005. Evaluation of global wind power. Journal of Geophysical Research D: Atmospheres 110 (12), 1–20. https://doi.org/10.1029/2004JD005462.

Barrera, C., Losada, I.J., Guanche, R., Johanning, L., 2019. The influence of wave parameter definition over floating wind platform mooring systems under severe sea states. Ocean Engineering 172, 105–126. https://doi.org/10.1016/j.oceaneng.2018.11.018.

Benitz, M.A., Schmidt, D.P., Lackner, M.A., Stewart, G.M., Jonkman, J.M., Robertson, A., 2015. Validation of Hydrodynamic Load Models Using CFD for the OC4-DeepCwind Semisubmersible. Volume 9: Ocean Renewable Energy. https://doi.org/10.1115/OMAE2015-41045. V009T09A037.

Chakrabarti, S. (1995). Offshore structure modelling. *Applied Ocean Research*, 17(6), 391–392. https://doi.org/10.1016/s0141-1187(96)00012-0.

DNV-GL, 2010. Environmental conditions and environmental testing. In: INTELEC, International Telecommunications Energy Conference (Proceedings), 2, pp. 92–99. https://doi.org/10.1109/INTLEC.1993.388591 (October).

DNV-GL, 2011. Offshore Standard DNV-RP-H103 -Modelling And Analysis Of Marine Operations. *Det Norske Veritas, April* 150.

DNV-GL, 2015. In: OFFSHORE STANDARD DNV GL AS Position mooring. *July*, 114.

Duarte, T., Gueydon, S., Jonkman, J.M., Sarmento, A., 2014. Computation of wave loads under multidirectional sea states for floating offshore wind turbines. Proceedings of the International Conference on Offshore Mechanics and Arctic Engineering - OMAE 9B. https://doi.org/10.1115/OMAE2014-24148 (March).

Goda, Y., 2010. Random Seas and Design of Maritime Structures. World Scientific. https://doi.org/10.1142/7425 (Vol. 33).

Gueydon, S., Duarte, T., Jonkman, J.M., 2014. Comparison of second-order loads on a semisubmersible floating wind turbine. Proceedings of the International Conference on Offshore Mechanics and Arctic Engineering - OMAE 9A. https://doi.org/10.1115/OMAE2014-23398 (March).

Hall, M. & Goupee, A. (2015). Validation of a lumped-mass mooring line model with DeepCwind semisubmersible model test data. *Ocean Engineering*, 104, 590–603. https://doi.org/10.1016/j.oceaneng.2015.05.035.

Hasselmann, K., Barnett, T.P., Bouws, E., Carlson, H., Cartwright, D.E., Enke, K., Ewing, J.A., Gienapp, H., Hasselmann, D.E., Kruseman, P., 1973. Measurements of wind-wave growth and swell decay during the Joint North Sea Wave Project (JONSWAP). Ergänzungsheft 8-12.

Hsu, W. ting, Thiagarajan, K. P. & Manuel, L. (2017). Extreme mooring tensions due to snap loads on a floating offshore wind turbine system. *Marine Structures*, 55, 182–199. https://doi.org/10.1016/j.marstruc.2017.05.005.

Jonkman, J.M., Buhl, M.L.J, 2005. FAST User's Guide - Updated. https://doi.org/10.2172/15020796. August 2005.

Karimirad, M. & Moan, T. (2012). A simplified method for coupled analysis of floating offshore wind turbines. *Marine Structures*, 27(1), 45–63. https://doi.org/10.1016/j.marstruc.2012.03.003.

Kim, B. W., Hong, S. Y., Sung, H. G. & Hong, S. W. (2015). *Comparison of simplified model and FEM model in coupled analysis of floating wind turbine*. 5. https://doi.org/10.12989/OSE.2015.5.3.221.

Kvittem, M. I. & Moan, T. (2015). Time domain analysis procedures for fatigue assessment of a semi-submersible wind turbine. *Marine Structures*, 40, 38–59. https://doi.org/10.1016/j.marstruc.2014.10.009.

Li, X. & Zhang, W. (2020). Long-term fatigue damage assessment for a floating offshore wind turbine under realistic environmental conditions. *Renewable Energy*, 159, 570–584. https://doi.org/10.1016/j.renene.2020.06.043.

Liu, H.F., Bi, C.W., Zhao, Y.P., 2020. Experimental and numerical study of the hydrodynamic characteristics of a semisubmersible aquaculture facility in waves. Ocean Engineering 214, 107714. https://doi.org/10.1016/j.oceaneng.2020.107714 (June).

Masciola, M., Robertson, A.N., Jonkman, J.M., Coulling, A., Goupee, A., 2013. Assessment of the Importance of Mooring Dynamics on the Global Response of the DeepCwind Floating Semisubmersible Offshore Wind Turbine. 23th International Offshore and Polar Engineering 9, 359–368.

Ozbahceci, B.O., Takayama, T., Mase, H., Ergin, A., 2002. Occurrence Probability of Wave Grouping for Different Shapes of Wave Energy Spectra. Proceedings of the International Offshore and Polar Engineering Conference 12, 37–42 (January).

Pinkster, J.A., 1980. In: Low frequency second order wave exciting forces on floating structures.

Robertson, A., Jonkman, J.M., Masciola, M., 2014. Definition of the Semisubmersible Floating System for Phase II of OC4. Nrel/Tp-5000-60601. https://doi.org/10.1021/jp200953k.

Robertson, A.N., Jonkman, J.M., Masciola, M.D., 2014. Definition of the Semisubmersible Floating System for Phase II of OC4. Nrel/Tp-5000-60601. https://doi.org/10.1021/jp200953k.

Robertson, A. N., Jonkman, J. M., Wendt, F. & Goupee, A. J. (2016). *Definition of the OC5 DeepCwind Semisubmersible Floating System*. 44. https://doi.org/10.1007/s10436-006-0062-y.

Robertson, A. N., Wendt, F., Jonkman, J. M., Popko, W., Dagher, H., Gueydon, S., Qvist, J., Vittori, F., Azcona, J., Uzunoglu, E., Soares, C. G., Harries, R., Yde, A., Galinos, C., Hermans, K., De Vaal, J. B., Bozonnet, P., Bouy, L., Bayati, I., … Debruyne, Y. (2017). OC5 Project Phase II: Validation of Global Loads of the DeepCwind Floating Semisubmersible Wind Turbine. *Energy Procedia*, 137, 38–57. https://doi.org/10.1016/j.egypro.2017.10.333.

Saulnier, J.B., Clment, A., Falco, A.F.D.O., Pontes, T., Prevosto, M., Ricci, P, 2011. Wave groupiness and spectral bandwidth as relevant parameters for the performance assessment of wave energy converters. Ocean Engineering 38 (1), 130–147. https://doi.org/10.1016/j.oceaneng.2010.10.002.

Tran, T.T., Kim, D.H., 2018. A CFD study of coupled aerodynamic-hydrodynamic loads on a semisubmersible floating offshore wind turbine. Wind Energy 21 (1), 70–85. https://doi.org/10.1002/we.2145.

Ulverston, D., La, C., Telephone, a J.U.K., Site, W, 2010. w OrcaFlex Manual. Interface 44 (0), 1–429. https://www.orcina.com/webhelp/OrcaFlex/Default.htm.

Waals, O.J., 2009. The effect of wave directionality on low frequency motions and mooring forces. Proceedings of the International Conference on Offshore Mechanics and Arctic Engineering - OMAE, 289–298. https://doi.org/10.1115/OMAE2009-79412. 4(PART A).

Walsh, C., 2019. Offshore wind in Europe. Refocus 3 (2), 14–17. https://doi.org/10.1016/s1471-0846(02)80021-x.

Yang, J., He, Y. P., Zhao, Y. S., Shao, Y. L. & Han, Z. L. (2021). Experimental and numerical studies on the low-frequency responses of a spar-type floating offshore wind turbine. *Ocean Engineering*, 222 (December 2020), 108571. https://doi.org/10.1016/j.oceaneng.2021.108571.

Zhang, S., Ishihara, T., 2016. Effects of Multidirectional Sea States and Flexible Foundation on Dynamic Response of Floating Offshore Wind Turbine System. In: First International Symposium on Flutter and Its Application, pp. 729–738.